

Enhancing the Utility of Complex-Valued Functional Magnetic Resonance Imaging Detection of Neurobiological Processes Through Postacquisition Estimation and Correction of Dynamic B_0 Errors and Motion

Andrew D. Hahn,¹ Andrew S. Nencka,¹ and Daniel B. Rowe^{1,2*}

¹Department of Biophysics, Medical College of Wisconsin, Milwaukee, Wisconsin 53222

²Department of Mathematics, Statistics and Computer Science, Milwaukee, Wisconsin 53233

Abstract: Functional magnetic resonance imaging (fMRI) time series analysis is typically performed using only the magnitude portion of the data. The phase information remains unused largely due to its sensitivity to temporal variations in the magnetic field unrelated to the functional response of interest. These phase changes are commonly the result of physiologic processes such as breathing or motion either inside or outside the imaging field of view. As a result, although the functional phase response carries pertinent physiological information concerning the vasculature, one aspect of which is the location of large draining veins, the full hemodynamic phase response is understudied and is poorly understood, especially in comparison with the magnitude response. It is likely that the magnitude and phase contain disjoint information, which could be used in tandem to better characterize functional hemodynamics. In this work, simulated and human fMRI experimental data are used to demonstrate how statistical analysis of complex-valued fMRI time series can be problematic, and how robust analysis using these powerful and flexible complex-valued statistics is possible through postprocessing with correction for dynamic magnetic field fluctuations in conjunction with estimated motion parameters. These techniques require no special pulse sequence modifications and can be applied to any complex-valued echo planar imaging data set. This analysis shows that the phase component appears to contain information complementary to that in the magnitude and that processing and analysis techniques are available to investigate it in a robust and flexible manner. *Hum Brain Mapp* 33:288–306, 2012. © 2011 Wiley Periodicals, Inc.

Key words: fMRI; magnetic field estimation; artifact correction; complex-valued regression; temporal noise

Contract grant sponsor: NIH; Contract grant numbers: EB000215 and EB007827.

*Correspondence to: Daniel B. Rowe, Cudahy Hall, 313, PO Box 1881, Milwaukee, WI 53201-1881. E-mail: daniel.rowe@marquette.edu
Received for publication 10 June 2010; Revised 18 October 2010; Accepted 27 October 2010

DOI: 10.1002/hbm.21217

Published online 8 February 2011 in Wiley Online Library (wileyonlinelibrary.com).

INTRODUCTION

The state of the spin system and the magnetic environment in MRI has unique effects on the magnitude and phase portions of the complex-valued reconstructed image. Accordingly, in a functional magnetic resonance imaging (fMRI) time series, each signal component may contain different information pertaining to the changing system and environment encoded in its temporal response, which

can then be used to infer certain physiology and/or physiologic function. Analysis of only the magnitude is standard in traditional blood oxygenation level-dependent (BOLD) [Bandettini et al., 1993; Ogawa et al., 1990] fMRI, but the potential value of the phase signal for the study of brain function and physiology may be substantial.

For example, the hemodynamic phase response can provide useful information in BOLD fMRI. The phase offset caused by a change in blood oxygenation, flow, and/or volume is dependent on the vascular morphology [Hoozenraad et al., 1998; Menon, 2002] much more so than is the magnitude. The theory presented suggests that voxels containing relatively small, randomly oriented vessels will show little phase change as opposed to voxels with larger, more coherently oriented vessels where significant phase change is expected. This distinction could be used to distinguish voxels more likely to contain cortical neurons from a delocalized area with draining veins [Menon, 2002; Nencka and Rowe, 2007]. Recent findings indicate, however, that hemodynamic phase response occurs in areas of microvasculature as well, suggesting a bulk magnetization effect leading to a net-phase change [Feng et al., 2009; Zhao et al., 2007]. Although this could confound identification of large vessels, it also presents an opportunity to use this response to further the understanding of hemodynamic biophysics.

Phase may be even more useful in neuronal current MRI (ncMRI) for the direct detection of action potentials [Bandettini et al., 2005]. The induced magnetic field expected from such an event is small, but potentially large enough to noticeably disturb the system and be detected. Simulations have shown that a larger phase than magnitude effect is expected [Heller et al., 2007], and phantom studies have come to similar conclusion [Bodurka and Bandettini, 2002; Bodurka et al., 1999]. Although an *in vitro* experiment showed promising results suggesting a detectable ncMRI signal [Petridou et al., 2006], much of the work published in the literature to this point has failed to demonstrate robust or undeniable detections *in vivo* [Chow et al., 2006; Konn et al., 2004]. However, recent results reported by Sundaram et al. [2010] appear more promising.

The lack of complex-valued BOLD fMRI used in practice and the lack of firm success or failure with ncMRI can be partially attributed to phase instability, which has been recently investigated by Hagberg et al. [2008]. Their results indicate that the presence of physiological noise tends to be more detrimental to phase than magnitude in terms of temporal standard deviation of phase (tSD_{ϕ}) and magnitude temporal signal-to-noise ratio (SNR). Although physiologic noise is certainly detrimental in both magnitude and phase, the particularly sensitive nature of the phase to these phenomena often renders it of little use in statistical analysis.

Using the sensitivity of the phase robustly and repeatedly as an investigative tool requires improved signal quality through reduction of the effects of noise described

earlier. This ideal signal would consist of the smallest independently and identically distributed white Gaussian noise as well as the largest evoked signal response possible. Any other structured signal confounds detection of the desired response unless properly modeled. Identifying the ideal pulse sequence parameters and using multiple receiver coils can help minimize noise and maximize response, while applying postacquisition modeling techniques can either provide direct stabilization or attempt to compensate for nuisance signals. A recently developed dynamic magnetic field map estimation and correction postprocess [Hahn et al., 2009] appears to be capable of compensating for signal likely caused by larger spatial scale temporal fluctuations in magnetic field. This was shown to significantly reduce phase variance and magnitude signal correlated with the field dynamics. By restricting the spatial variability of the estimated field, spatially local changes remain unaffected, only removing dynamics on larger spatial scales.

Appropriate statistical modeling is also important for the detection of functional response. A line of research involving complex-valued regression models has been described in the literature [Lai and Glover, 1997; Lee et al., 2007; Nan and Nowak, 1999; Rowe and Logan, 2004, 2005; Rowe, 2005a,b, 2009], and each is appropriate in certain situations. In general, these models fall into two separate categories: the magnitude and phase signals are either uncoupled, as in the case of Lai and Glover [1997] as well as in Lee et al. [2007], or coupled appropriately as in Nan and Nowak [1999], Rowe and Logan [2004, 2005], and Rowe [2005b, 2009]. These models are only appropriate whenever the phase data represent relevant information, that is, is dependent on the state of an input of interest. Examples of situations where phase has a relevant response are discussed earlier, and results will be presented below supporting a physiological relationship between the phase and task performance. When used appropriately, complex-valued regression models provide the inherent benefit of increasing statistical power simply by using twice as many data values as a scalar alternative [Rowe, 2005a]. Inappropriate tests with irrelevant phase data will in fact be less powerful than if phase was excluded altogether. The complex-valued model can be designed to detect task-related phase changes in addition to task-related magnitude changes [Rowe, 2005b], thereby increasing the possible circumstances under which activation is detected for a given SNR and contrast-to-noise ratio [Hernandez-Garcia et al., 2009]. Furthermore, by operating on real and imaginary data, the potential problems with magnitude and phase distributions at low SNR, which approach Raleigh and uniform distributions, respectively [Rowe and Logan, 2004; Zhu et al., 2009], are avoided. Data analysis was performed with the model from Rowe [2005b] in this work. It is the most flexible, allowing separate, arbitrary design matrices for the magnitude and phase; however, it is also more

computationally intensive. This computational complexity can be spared in certain, more restricted situations. It is worth emphasizing that using a complex-valued approach *requires* an expected response reference for both magnitude and phase, and very poorly chosen phase responses can limit its usefulness. When this is the case, it may be appropriate to analyze only the magnitude data [Bandettini et al., 1993; Rowe and Logan, 2005; Rowe, 2005a] using a general linear model (GLM). Analysis of only the phase might also be appropriate, either with the same technique (in the absence of wrap-around) or with a more advanced angular regression model [Rowe et al., 2007]. Clearly, the statistical advantages of the joint magnitude and phase complex-valued methods would be sacrificed.

As an alternative to using a GLM for complex-valued statistical analysis, a method for independent component analysis (ICA) of complex-valued data has been provided by Calhoun et al. [2002]. Like all ICA techniques, the algorithm does not require regressors a priori like the GLM, but rather generates them from the signal itself under linear independence constraints. This provides certain advantages, most notably that the response to input can be unknown, which is not feasible with a GLM. For the purposes of this work, ICA is not appropriate for this precise reason. The need to include or exclude certain regressors such as estimated motion parameters led to the choice of a GLM.

The work reported in Hahn et al. [2009] presented the framework for the temporal off-resonance alignment of single-echo time series (TOAST) method and showed its usefulness with regard to phase stabilization and use with the complex constant phase-statistical model [Rowe and Logan, 2004]. The results presented here aim to extend that work in two ways: (1) by evaluating the addition of nuisance regression using estimated motion parameters [Johnstone et al., 2006] to the complex-valued postprocessing pipeline, and (2) by demonstrating the potential to repeatedly provide access to physiologic information embedded in the phase of the complex-valued fMRI signal that may be otherwise practically undetectable, rather than simply the ability to provide phase stabilization. Specifically, the most general complex-valued statistical model of Rowe [2005b] is used to show improved detection ability in both magnitude and phase as opposed to simply demonstrating improved detection in magnitude assuming temporally constant phase. This is accomplished by first demonstrating this ability in human experimental fMRI time series. Additionally, the effect of the dynamic field corrections and nuisance regression on the magnitude and phase stability in terms of the variance, autocorrelation, and distribution of the residuals after regression is presented. This is followed by similar analysis of simulated fMRI data to provide verification of the experimental results. The reliability provided by these techniques makes complex-valued analysis more applicable to general studies, presents greater opportunity to measure, and uses all the fMRI data acquired to investigate various physiologic processes.

MATERIALS AND METHODS

Data Acquisition

All experimental fMRI data were acquired using a GE Signa LX 3T scanner (General Electric, Milwaukee, WI) using the stock quadrature head receiver coil, and functional images were collected with a single-shot echo planar imaging (EPI) pulse sequence. Three separate fMRI experiments were performed and will be referred to as EXPB, EXPJ, and EXPC. The pulse sequence parameters for each experiment are shown in Table I. The first two experiments were performed during the same scanning session, while the third was collected at a later date with typical parameters.

The human subject was scanned after providing informed consent using a protocol approved by the Medical College of Wisconsin Institutional Review Board. During all the experiments, the subject performed a bilateral finger tapping task in a block design pattern, and on/off signaling was provided with a visual cue. For experiments EXPB and EXPJ, the block design pattern consisted of 16 blocks of 8 s of stimulus and 8 s rest, all following a 20-s initial rest, while EXPC had only 10 blocks of 8 s of stimulus and 8 s rest, all following a 20-s initial rest. EXPB and EXPJ also introduced intentionally suboptimal conditions to emphasize the types of often occurring phenomena that

TABLE I. Pulse sequence parameters and tasks for each fMRI experiment

	EXPB	EXPJ	EXPC
No. of slices	9	9	9
Matrix size	96 × 96	96 × 96	64 × 64
TE (ms)	42.8	42.8	26.0
TR (s)	1.0	1.0	1.0
Flip angle	45°	45°	45°
Bandwidth (kHz)	125	125	125
Echo spacing (ms)	0.768	0.768	0.680
Field of view (cm)	24	24	24
Slice thickness (mm)	2.5	2.5	3.8
Repetitions	296	296	180
No. of alternating TEs ^a	20	20	0
Functional task	Finger tap	Finger tap	Finger tap
Nuisance task ^b	Deep breath	Jaw motion	None

^aOdd-numbered images have a 5-ms longer TE.

^bTask performed at 0.167 Hz rate.

can confound statistical analysis. This was accomplished using a secondary “nuisance” task, intended to induce an elevated yet reasonable amount of signal instability, and performed simultaneously with the finger tapping task. In EXPB, the same subject was instructed to breath deeply at a 0.167 Hz rate for the duration of the experiment, and a timing reference indicating when to inhale and exhale was provided visually along with the finger tapping cue. Experiment EXPJ replaced the heavy breathing with periodic jaw movement at the same frequency. Specifically, the subject was given the same timing cue as provided to keep breathing consistent, but with breath in/out replaced by open/close mouth. For experiment EXPC, the subject was asked to perform the stimulus task only, with no nuisance task, and to remain as still as possible otherwise.

It is also important to note that, for experiments EXPB and EXPJ, the TE was lengthened by 5 ms on odd-numbered repetitions during acquisition of the first 20 repetitions to provide an initial absolute magnetic field map reference, $\Delta\omega_0$, to be used as described below. These additional images were discarded before statistical activation analysis. This was not done for EXPC.

The results to follow are focused on analysis of EXPB and EXPJ to provide consistency of sequence parameters and experimental design (other than the nuisance task) across the data from which conclusions may be drawn. However, it is worthwhile to similarly investigate a situation representing more typical fMRI experimental conditions, and this purpose is served by EXPC. The results of this analysis are left for the Discussion section of this document and are thus considered for the purposes of discussion only.

Reconstruction and Dynamic Magnetic Field Correction

All acquired image data were reconstructed offline from raw GE p-files. Data processing required for image reconstruction and correction of magnetic field dynamics was done with a custom program written in C and designed in-house. The process flow involved image generation from k -space by inverse Fourier transform, Nyquist ghost removal [Jesmanowicz et al., 1993], estimation of the dynamic field using TOAST [Hahn et al., 2009], and finally correction of the images with field maps calculated from the first 20 repetitions.

The method for estimating the main magnetic field offset at each time point t , $\Delta\omega_t$, from time variant portion of the main magnetic field off-resonance, $\delta\omega_t$, and an initial absolute reference, $\Delta\omega_0$, is described by Hahn et al. [2009] and is applicable to single-shot gradient echo EPI (GE-EPI) pulse sequences. The calculation can be written as

$$\Delta\omega_t = \frac{\arg\left\{I_t \sum_{k=1}^{N-1} \frac{I_k}{|I_k|}\right\} - \arg\left\{I_0 \sum_{j=1}^{N-1} \frac{I_j}{|I_j|}\right\}}{\text{TE}} + \Delta\omega_0 \quad (1)$$

For a series of N images where I_t is the reconstructed complex-valued image at time t , TE is the echo time, $*$ denotes complex conjugation, and the arg operator returns the phase angle of its argument. It is worth noting that $\Delta\omega_0$ is not required to correct the field dynamics, but without it, absolute field correction is not possible, and thus registration of the functional data to T_1 -weighted anatomical images is not reliable.

The raw field maps were processed to reduce noise, control nonactivation related high-spatial frequency information captured by the field map, and reduce estimation artifacts at the image boundaries before being applied in the correction. This was accomplished by using a locally weighted least squares regression [Cleveland and Devlin, 1988]. The first step in this process was to censor voxels to be used in the fitting procedure. A binary mask of voxels above 7% of the maximum voxel magnitude was generated, representing voxels within the brain. Voxels well outside the brain were selected by dilating the original mask by 10 voxels and then inverting it. These voxels had the value of the estimated field (originally only noise) set to zero. This caused the fit of the raw estimated field to fall to zero outside the brain. The voxels not contained within either of these two masks were censored and not used in the fitting procedure.

The next step involved moving voxel-by-voxel over the entire image and fitting a weighted two-dimensional polynomial using the 20% of all noncensored voxels, which are closest (by Euclidean distance) to the current voxel. After selecting the closest 20% of voxels, a tri-cube weight function is used to weight each point according to its distance from the current point. The weight for the j th point, w_j , is found using

$$w_j = \left(1 - \left(\frac{d_j}{d_{\max}}\right)^3\right)^3, \quad (2)$$

where d_j is the Euclidean distance between the current voxel and the j th voxel, and d_{\max} is the maximum Euclidean distance between the current voxel and a voxel within the closest 20% of noncensored voxels. The two-dimensional polynomial coefficients were fit using weighted least-squares according to

$$P = (X^T W X)^{-1} X^T W Y. \quad (3a)$$

The j th row of X is x_j , and $d_{x,j}$ and $d_{y,j}$ are the distance from the current voxel in the x -direction and y -direction of the j th voxel, respectively.

$$x_j = \left[1 \quad d_{x,j} \quad d_{x,j}^2 \quad d_{y,j} \quad d_{y,j}^2\right] \quad (3b)$$

where W is a diagonal matrix, the j th diagonal element of which is w_j from Eq. (2). P is a five-element vector containing the polynomial coefficients.

Once the coefficients for the fit were computed at a specific point, the value of the processed estimated field at that point was calculated. It should be noted that the estimated value of the voxel of interest is simply the first element of P , because the distance from itself is clearly zero in each direction (i.e., designed to be located at position $x = y = 0$).

Once this processing has been carried out, the field maps were applied using the one-dimensional (phase-encoding direction) simulated phase rewinding [Kadah and Hu, 1997] correction method to remove their effects from the original images.

As a final processing step, the angular mean [Rowe et al., 2007] of each voxel time series following the dynamic field correction was subtracted out to prevent phase wrapping within the imaged object. No voxels inside the object drifted more than 2π radians over the length of the experiment, especially after being corrected for the field dynamics, and zeroing that the mean was sufficient in all cases to prevent wraparound in voxels within the head.

Simulation

Simulations were performed to supplement and verify the results obtained from the human fMRI experiments described earlier. The simulator is designed to emulate the acquisition of k -space as would occur in an actual scan session. Generation of a single image (slice) requires two conceptually separate configuration specifications. First, certain properties of both the object to be “scanned,” and the magnetic environment within the space occupied by the object must be provided. These include two-dimensional spatial maps of spin density, $\rho(x,y)$, tissue transverse relaxation $T_2^*(x,y)$, and the magnetic field offset from resonance (resonance defined as 3.0 T), $\Delta B_0(x,y)$. The second configuration concerns the scanning parameters for the k -space acquisition itself (limited to GE-EPI), which

include echo time, field of view, image matrix size, and sampling bandwidth. These parameters provide the necessary information for the simulator to create x and y gradient waveforms (150 mT/m/s peak slew rate and 40 mT/m peak amplitude), G_x and G_y , emulating those which would be generated by an actual scanner given the specified input. Finally, sampling times, $m_{k_x, k_y} \Delta t$, are associated with each sampled k -space point and the “acquired” signal for the j th image in a time series, S_j , is produced according to

$$S_j(m\Delta t) = \sum_{q=-\frac{N_x}{2}}^{\frac{N_x}{2}-1} \sum_{r=-\frac{N_y}{2}}^{\frac{N_y}{2}-1} \rho(q\Delta x, r\Delta y) e^{\left(\frac{m\Delta t}{T_2^*(q\Delta x, r\Delta y)}\right)} \dots \times e^{i\gamma\Delta t \left[\sum_{w=0}^m (G_x(w\Delta t)\Delta x + G_y(w\Delta t)\Delta y) + m\Delta B_0(q\Delta x, r\Delta y) \right]} \quad (4)$$

In the above equation, Δx and Δy are the spatial dimensions represented by a single point in the $N_x \times N_y$ point input parameter maps ρ , T_2^* , and ΔB . The simulations presented in this work used $\Delta x = \Delta y = 468.75 \mu\text{m}$ and $N_x = N_y = 512$. The variable Δt represents the timing resolution of the gradient waveforms (*not* the sampling rate). The value of Δt can be any divisor of the sample rate, and the smaller its value, the closer the gradient sum over m approximates the continuous integral over time $m\Delta t$ (0.1 μs used here).

Three separate series of 296 ($0 \leq j < 296$) single-slice images were simulated containing areas of locally induced temporal signal change designed to mimic a functional response and will be referred to as SIMB, SIMJ, and SIMC. The SIMB and SIMJ series were created using a temporally variant ΔB field and simulated motion in an attempt to emulate similar effects in EXPB and EXPJ, while the SIMC series contained neither and is intended to serve as a control.

The $\rho(x,y)$ parameter map, shown in Figure 1a, was the same for all three series and was created using a slice from the reconstructed images from EXPB after it had been corrected for magnetic field inhomogeneity. The magnitude of the original image was sinc interpolated to dimensions of 512×512 and then masked to zero everywhere outside of the brain. The simulated functional responses, also identical in each, were induced by increasing the value of T_2^* and either increasing or decreasing the value of ΔB during task to elicit magnitude and phase changes, respectively. The variations were applied in a block design pattern identical to that used for the finger-tapping task in EXPB and EXPJ. The map of ρ and the locations containing these local variations are shown in Figure 1b, and each active area is a 13×13 square, measuring 6.1 mm on a side. The values of T_2^* and the portion of ΔB associated with local activity at each location are shown for task “off” and task “on” periods in Table II. During task “off” periods and everywhere outside of the active locations, T_2^* is equal to 35 ms and the local ΔB is equal to 0.

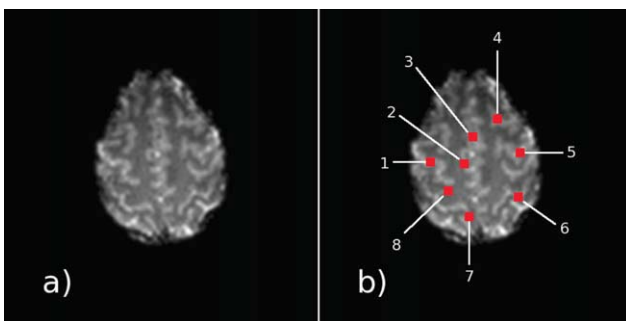


Figure 1.

The ρ map used as input to the simulation (a). The same map is shown in (b), overlaid by the locations where activation was simulated in either magnitude, phase, or both. The type and size of the simulated activity can be found for each numbered location in Table II. [Color figure can be viewed in the online issue, which is available at wileyonlinelibrary.com.]

TABLE II. Local values of T_2^* and ΔB during both task “off” and task “on” periods at locations one through eight

Location	1	2	3	4	5	6	7	8
T_2^* (ms), task “off”	35.0	35.0	35.0	35.0	35.0	35.0	35.0	35.0
T_2^* (ms), task “on”	35.35	35.7	35.0	35.35	35.7	36.05	35.35	36.05
ΔB (nT), task “off”	0.0	0.0	0.0	0.0	0.0	0.0	0.0	0.0
ΔB (nT), task “on”	2.83	-4.25	2.83	0.0	1.42	-2.83	4.25	1.42

The area to which each refers is shown in Figure 1b.

The SIMB and SIMJ series were generated with simulated bulk motion. The amount of motion to apply was determined directly from the estimations of the motion made with the AFNI [Cox, 1996] plug-in 2dImReg from EXPB for SIMB and EXPJ for SIMJ. The simulated motion was implemented by shifting and rotating the ρ , T_2^* , and local activation related ΔB maps, discussed above, by the appropriate amount at each time point, j , before applying Eq. (3).

In addition to the ΔB map for inducing phase activation-related response, each simulated image series contained an additional magnetic field offset representing bulk field inhomogeneity. In SIMC, a temporally static field was applied, and it was generated using the static field ($\Delta\omega_0$) estimated for EXPB following interpolation to dimensions of 512×512 , similarly to the ρ map. SIMB and SIMJ were generated using the sum of the same map used for SIMC, and the series of dynamic reference field maps ($\delta\omega_t$ from Hahn et al. [2009] estimated for EXPB and EXPJ, respectively, also interpolated to 512×512 . It should be noted that this portion of the ΔB was not included in the motion simulation process, because it was assumed that it already contained the changes, which occurred due to any motion that occurred. The full ΔB map that was finally applied in Eq. (3) was the sum of this bulk field inhomogeneity map and the local activation field map (after having motion applied, if applicable).

A static magnetic field offset was applied to all three series as well. This field was simply the static field estimation from EXPB (nearly identical to that in EXPJ) following interpolation to dimensions of 512×512 , similarly to the $\rho(x,y)$ map. The additional temporally dynamic fields used for SIMB and SIMJ were generated directly from those estimated in EXPB and EXPJ, respectively, again interpolated to a 512×512 matrix.

Besides the already specified parameters, each series was simulated with identical scan parameters to EXPB and EXPJ above, with the exception of the echo spacing, which was $759 \mu\text{s}$ in the simulation. This includes the images with extended echo time during the initial 20 repetitions. The difference in echo spacing from that in the actual experimental data ($768 \mu\text{s}$) was due to round-off errors in the calculation method of the simulated gradients. This small $9\text{-}\mu\text{s}$ difference should not be of any consequence.

Finally, once all three of the simulated image series were generated, each was duplicated 100 times and inde-

pendently, and identically distributed Gaussian random noise was added to the real and imaginary channels of the k -space samples. The variance of the added noise, equal to 10, was scaled such that the SNR of the reconstructed images was similar to that in EXPB and EXPJ, which were ~ 20 within the brain. Each image series was then processed in an identical manner to the human results.

Statistical Modeling and Analysis

The complex-valued generalized likelihood ratio detection model used is described in detail in Rowe [2005b], but will be summarized for clarity. The general form of the complex-valued multiple regression model, assuming a series of n complex-valued images and using notation similar to the original work, is

$$y_t = [p_t \cos \theta_t + \eta_{\text{Rt}}] + [p_t \sin \theta_t + \eta_{\text{It}}] i \quad (5a)$$

$$r_t = \sqrt{y_{\text{Rt}}^2 + y_{\text{It}}^2}, \quad \phi_t = \arctan\left(\frac{y_{\text{It}}}{y_{\text{Rt}}}\right) \quad (5b)$$

$$\theta = \mathbf{U}\gamma. \quad \rho = \mathbf{X}\beta \quad (5c)$$

where $(\eta_{\text{RT}}, \eta_{\text{IT}})' \sim N(0, \Sigma)$, $\Sigma = \sigma^2 I$, and ρ_t and θ_t are the true magnitude and phase elements of ρ and θ at time t , and y_t is the *observed* complex-valued signal at time t , also represented as magnitude, r_t , and phase, ϕ_t . Additionally, assuming that s slices are acquired, and each image has dimensions $h \times w$, r , and ϕ are $n \times (hws)$ matrices containing the magnitude (former) and phase (latter) measurements from an individual voxel in each column. The $n \times (q_1 + 1)$ matrix \mathbf{X} and the $n \times (q_2 + 1)$ matrix \mathbf{U} contain magnitude and phase regressors (besides a mean regressor) column-wise, and the corresponding coefficients in each voxel fill the columns of the $(q_1 + 1) \times (hws)$ matrix β and the $(q_2 + 1) \times (hws)$ matrix γ .

Four hypothesis conditions are described by Rowe [2005b], which can be used to formulate a variety of statistical tests on the regression coefficients. The aforementioned hypotheses are $H_a: \mathbf{C}\beta \neq 0, \mathbf{D}\gamma \neq 0$, $H_b: \mathbf{C}\beta = 0, \mathbf{D}\gamma \neq 0$, $H_c: \mathbf{C}\beta = 0, \mathbf{D}\gamma \neq 0$, and $H_d: \mathbf{C}\beta = 0, \mathbf{D}\gamma = 0$ with linear constraint matrices for magnitude, \mathbf{C} (r_1

$\times (q_1 + 1)$), and phase, D ($r_2 \times (q_2 + 1)$). Using these in proper combination of null and alternative hypotheses makes tests for arbitrary magnitude or phase response either with, without, or regardless of a response (also arbitrary) in the other signal component possible and provides all necessary capabilities for the analysis to follow.

After estimating the regression coefficients under both the null and alternative hypothesis, a distributed general likelihood ratio test statistic, $-2 \log(\lambda)$, can be computed using the variance of the residual error of the least squares fit for the null, $\hat{\sigma}^2$, and alternative, $\hat{\sigma}^2$, hypotheses as

$$\sigma^2 = \frac{1}{2n} [(\mathbf{r} - \mathbf{X}\beta)^T(\mathbf{r} - \mathbf{X}\beta) + 2(\mathbf{r} - \mathbf{r}_s)^T \mathbf{X}\beta]$$

$$-2 \log(\lambda) = 2n \log \left(\frac{\hat{\sigma}^2}{\hat{\sigma}^2} \right) \quad (6)$$

The degrees of freedom, r , in the test statistic is dependent on the specific hypotheses being tested. A comparison of either H_b versus H_a or H_d versus H_c gives r equal to r_1 , the full row rank of C, while H_c versus H_a or H_d versus H_c tests yield r equal to r_2 , the full row rank of D. If comparing the H_d and H_a hypotheses, the test statistic has $r_1 + r_2$ degrees of freedom.

The stimulus reference function, $f_{\text{stim}}(t)$, was modeled here by a function that is simply -1 during task-off periods and 1 during task-on periods, shifted by an amount $\delta t_h = 4$ s to account for hemodynamic delay. The shifted boxcar was chosen as opposed to a more elaborate reference curve, for example, the boxcar convolved with a gamma function, for the sake of simplicity and consistency. The relative accuracy of a boxcar and an alternative model function is not well known with respect to the phase response and will likely vary with location. Unless otherwise stated, the design matrices X and U were the same, with a column of 1s (mean regressor), a column with a linear ramp from -1 to 1 (linear trend regressor), and a column containing $f_{\text{stim}}(t - \delta t_h)$, effectively treated as the response model in this case. The test contrast matrices C and D have a single row of 0s with a single 1 in the column of X or U, respectively, containing $f_{\text{stim}}(t - \delta t_h)$ (C = D).

Regression analysis of both magnitude-only and phase-only data was also used for the purposes of comparison, both of which are special cases of the model described above. To test the magnitude-only hypothesis, X remains as described earlier, and the phase is left unconstrained under both null and alternative hypotheses (H_b vs. H_a), with U equal to an $n \times n$ identity matrix I_n . (The constraint matrix D is not used in the computation, because phase is unconstrained under H_b and H_a .) Similarly, allowing unconstrained magnitude under both hypotheses (H_b vs. H_a) with X equal to I_n performs a test of the phase-only with U unchanged (the constraint matrix C is unused in this case).

RESULTS

Human

Regression analysis using the complex-valued model was performed on both fMRI time series after correction of only a static magnetic field inhomogeneity using $\Delta\omega_0$ as well as dynamic magnetic field errors using $\Delta\omega_t$. Estimates of the motion in two axes of translation and one of rotation were made using the AFNI plug-in 2dImReg, also before and after each type of field correction. Motion compensation, when used, was applied by including the temporal motion estimates as additional regressors in the design matrices X and U. Specifically, motion estimates made before applying field correction were used as regressors in X and U when computing activation in the time series of images that was not corrected for temporal magnetic field variations (motion correction only case). On the other hand, estimates of motion made after field correction were used to compute activation in the images that were corrected for temporal magnetic field variations (motion and field correction case). The series of images were *not* shifted or rotated at all using the motion estimates. The motivation for this analysis method will be discussed in the Discussion section to follow. The term motion correction or motion compensation will be used in the remainder of this analysis to refer to the inclusion of the motion estimates as additional regressors as described here and not as rigid body rotation and translation. This process yields the results of four processing types: none, motion compensation only, dynamic field correction only, and dynamic field correction and motion compensation. Static magnetic field correction is implied in the all four types.

Maps of $-\log_{10} P$ where P is the P -value associated with the test statistic at a unadjusted threshold [Logan and Rowe, 2004; Logan et al., 2008] in a single slice from EXPB and EXPJ after each combination of processing steps are shown for tests of the magnitude-only, phase-only, and magnitude-and-or-phase in Figure 2. The anatomic underlay in each of these figures, and in the figures to follow, is the first image in the functional EPI time series. The hypotheses for the test of magnitude-and-or-phase are, and all other parameters for each test, described in the Methods section of this document.

The different postprocesses appear to have only a slight impact on the magnitude-only activation detection, as evident from Figure 2a,b, which show a single slice from EXPB and EXPJ with the processing combinations along the columns. This is not unexpected, and is in agreement with previous results reported by Hahn et al. [2009], which analyzed the effect of the dynamic field correction and motion on the magnitude signal component and magnitude-only activations in some detail. This is especially true of the results of EXPB (Fig. 2a), which involves the heavy breathing nuisance task and shows very little difference between the four different processing cases. The results of EXPJ (Fig. 2b) show somewhat more significant

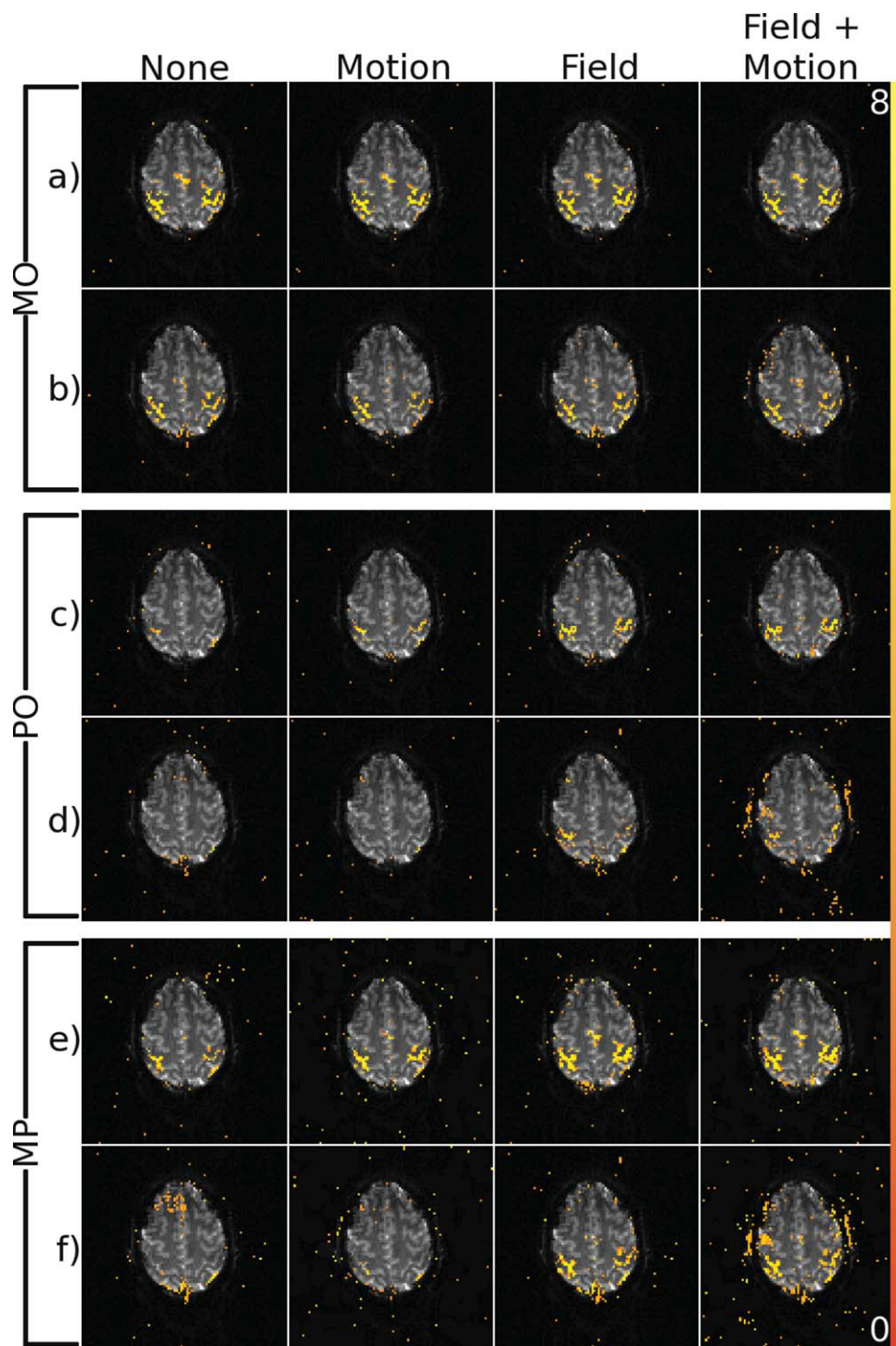


Figure 2.

Maps of $-\log_{10}(P)$ where P is the P -value associated with the χ^2 statistics for magnitude-only (a,b), phase-only (c,d), and magnitude-and-or-phase (e,f) activation. The results of EXPB (a,c,e) and EXPJ (b,d,f) are shown for each activation model. From left to right, columns show results after no postprocessing, motion

compensation only, dynamic field correction only, and both motion and field correction. Active voxels shown above a threshold of $P < 5 \times 10^{-4}$ (unadjusted). [Color figure can be viewed in the online issue, which is available at wileyonlinelibrary.com.]

differences, especially in the cases including motion compensation. Including motion correction appears to reduce the amount of detected activity, although there are a few areas where activity may be increased with its inclusion.

The phase-only activations clearly show that the different postprocessing steps affect the detection of activation response in the phase signal (Fig. 2c,d). In both experiments, the number of active voxels and their relative significance is elevated following any postprocessing compared to none at all, with the exception of using motion compensation alone in EXPJ. This is significant in that the applied corrections not only stabilize the phase signal by removing spatially global variation, as was demonstrated by Hahn et al. [2009], but additionally preserve spatially local variations and increase the detection power of task related signal of potential interest. In EXPB, results indicate that TOAST correction alone appears to allow for better activity detection than only motion compensation; however, it is difficult to discern whether the application of both provides additional improvement or not due to the relative similarity between the activated regions when using the field only and when using both the field and motion in the correction.

The analysis of EXPJ (Fig. 2d) indicates similar benefit from using only the field correction as in EXPB, but performing motion compensation in this case yields somewhat different results. As previously mentioned, motion correction alone has very little effect on the phase-only activity. However, when applied in conjunction with TOAST, an activation pattern results, which is different in certain respects from what is shown using just TOAST. Specifically, when both corrections are applied, significant activity is detected in the skull region on both the left and right sides, and some additional activity is detected within the brain as well on the left side. The uniqueness and questionable anatomical relevance of this detected activity with respect to the finger tapping functional task suggest that it is of an artifactual nature. This artifact may be related to the jaw motion occurring during acquisition, due to its location above the jaw bone, and the affect of this motion on the main magnetic field [Birn et al., 1998]. Detection of false-positive activity has been described by Soltysik and Hyde [2006] in the presence of similar jaw motion associated with chewing. In that case, however, the jaw motion was directly related to the task of interest, opposed to this case where the functional task and jaw motion occur at different frequencies. However, an additional factor could potentially be instability of the motion compensation regression model resulting from multicollinearity of the design matrix columns, which include motion parameters.

The degree of multicollinearity in the independent variables of the linear model including the motion estimates in EXPJ was evaluated by using the condition number of the matrix. This value is defined as the square root of the ratio of its largest to smallest singular values and provides information about the linear independence of the matrix's

columns. An orthogonal matrix has a condition number of one and a matrix containing one or more columns, which are a perfect linear combination of the other columns, has a condition number of infinity. The condition number without including motion parameters is 3.46, while including motion yields a condition number of 30.33 and 23.02. The literature states that a condition number of 10 represents the low end of where collinearity starts to affect the solution, while a condition number of 100 indicates serious effects of collinearity [Belsley et al., 1980]. The model including motion is well into this range; thus, multicollinearity may be causing instability.

The results provided in Figure 2e,f present little surprise given the magnitude-only and phase-only activations in Figure 2a–d. However, it is apparent that the activated locations are understandably not simply a combination of the magnitude-only and phase-only activations. The differences arise from the fact that the uncertainty of the overall fit in this case involves a combination of the uncertainty in both the magnitude and phase [Rowe and Nencka, 2006]. Intuitively, in the unprocessed data, the large phase variations cause increased uncertainty nearly uniformly, resulting in a loss of significance where activations in the magnitude were previously apparent. This “grouped” variation can become beneficial; however, if both magnitude and phase are properly modeled. In this case, the overall variation of both magnitude and phase is less than either alone, due to the increased number of data values, thus leading to significant detection of response which otherwise is too small. As a result, the magnitude-and-or-phase activations can be a superset of the magnitude-only and phase-only activations and have greater significance where overlap occurs.

One notable characteristic of these results is the apparent difference between the activity detected in EXPB and EXPJ, given that the only difference between the two is the type of nuisance task being performed. Specifically, the size and significance of the activation seems greater in EXPB in both magnitude and phase even after full correction. The most likely reason for this are differences in the amount and type of motion present during each experiment. First, maintaining head position when opening and closing the mouth is a greater challenge than doing so during heavy breathing, and this was represented in the computed motion parameters in all three axes. The variance of the displacement in EXPB (for repetitions 31–296, the same set used for regression analysis) was millimeter left-to-right, millimeter anterior-to-posterior, and degrees rotation around the inferior–superior axis, compared to millimeter, millimeter and degrees in EXPJ, each of which is significantly larger than the corresponding variance in EXPB when using an *F*-test ($P < 0.001$). Besides containing greater amounts of bulk motion, the close proximity of the jaw motion in EXPJ to the imaging plane results in variable subvoxel field gradients and thus variable signal dropout. This is not correctable using TOAST and is not necessarily associated with bulk motion, although there is likely a correlation between

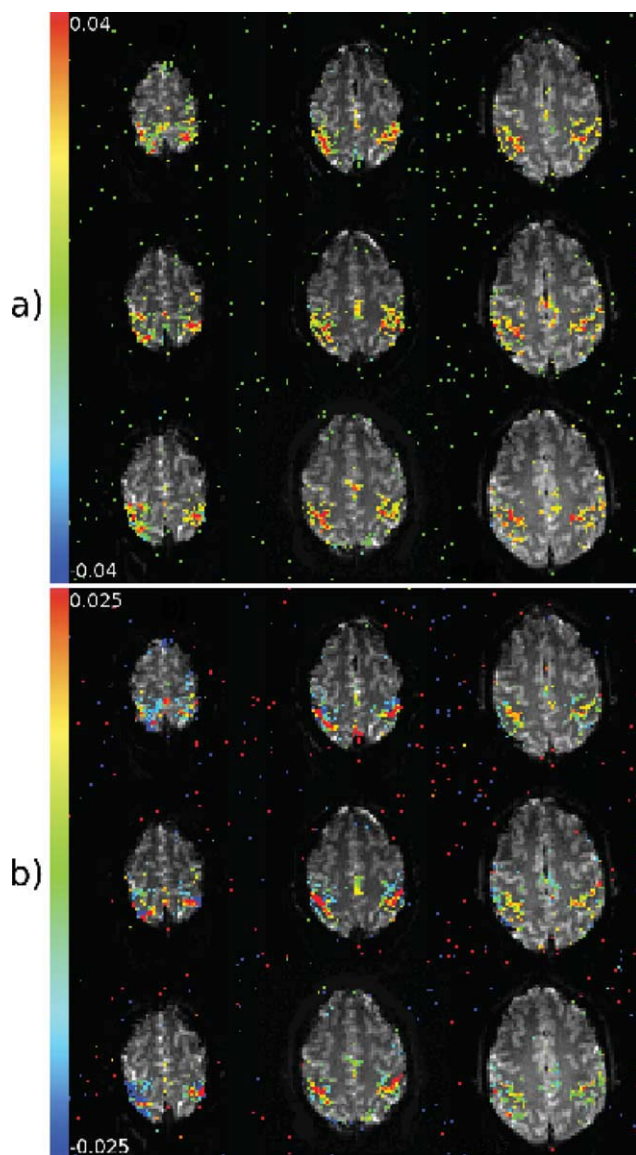


Figure 3.

All slices from EXPB after dynamic field and motion correction are shown with overlays of β_{ref} (a) and γ_{ref} (b), calculated from the complex-valued regression test. The coefficients are shown where the χ^2 of the overall test was significant with $P < 5 \times 10^{-4}$ (unadjusted). [Color figure can be viewed in the online issue, which is available at wileyonlinelibrary.com.]

the two. Regardless, this phenomenon almost certainly decreases sensitivity of activation detection.

The data presented so far indicates that statistical tests for the presence of a task-related signal component in the magnitude, phase, or both has significantly more power after applying the processing. It is somewhat apparent by comparison of the statistics in Figure 2a,b with those in and 2c,d that there is a different pattern of activation in

magnitude and phase and thus potentially different physiologic information. However, the complex-valued regression more appropriately models the two components in tandem, as described by Rowe [2005b] as well as Statistical Modeling and Analysis Section of this document and thus theoretically presents a better representation of the joint response through more accurate coefficient estimates. The individual response characteristics of the magnitude and phase, in addition to the relationship between them, can be visualized with more clarity in Figure 3. Here, all slices from the fully postprocessed experiment EXPB data set are shown with overlay maps of β_{ref} (Fig. 3a) and γ_{ref} (Fig. 3b), the coefficients of the task reference regressor in the magnitude and phase, respectively. These coefficients are shown only where the overall test (χ^2) was significant to (unadjusted). Using this display method, locations with only magnitude activation are located where the phase coefficients displayed are nearly 0 and vice versa for locations with only phase activation. The fact that each contains unique information is apparent, and the most notable pattern seems to be the increasing strength of the phase response in the superior direction. Thorough and conclusive interpretation of these results is not the focus of this work, and this information is provided here as further evidence that such results are accessible and potentially meaningful.

To supplement the regression analysis, time series modeling of the real and imaginary regression residuals was performed to determine both the initial characteristics of voxel time series and the temporal stabilizing effects of the dynamic field mapping and nuisance signal regression. In an ideal situation, as assumed by the linear regression model, residual errors in the real and imaginary channels are temporally independent and normally distributed. The degree to which these assumptions are violated influences the interpretation of the significance of the test statistic and coefficient estimators [Luo and Nichols, 2003].

Voxel-wise tests for temporal independence of both real and imaginary residuals of the complex-valued regression after the different postprocessing steps are displayed for a single slice (the same slice as used for previous analysis) from each experiment in Figure 4. These figures show maps of $-\log_{10} P$, where P is the P -value associated with the statistic of a Breusch–Godfrey test [Breusch, 1979; Godfrey, 1978] for the presence of autocorrelations at a time lag of one, with voxels shown as significant above a threshold of $P < 0.001$ (unadjusted). The Breusch–Godfrey test is used instead of the Durbin–Watson test [Durbin and Watson, 1971], which is the test used by Luo and Nichols [2003] because of its insensitivity to deviations from normality of the samples. Results of these tests indicate that the presence of motion and a temporally dynamic magnetic field offset both influence the temporal independence of the residuals to varying degrees, which is an expected result. This is evident from the fact that neither the field nor motion correction alone is generally sufficient

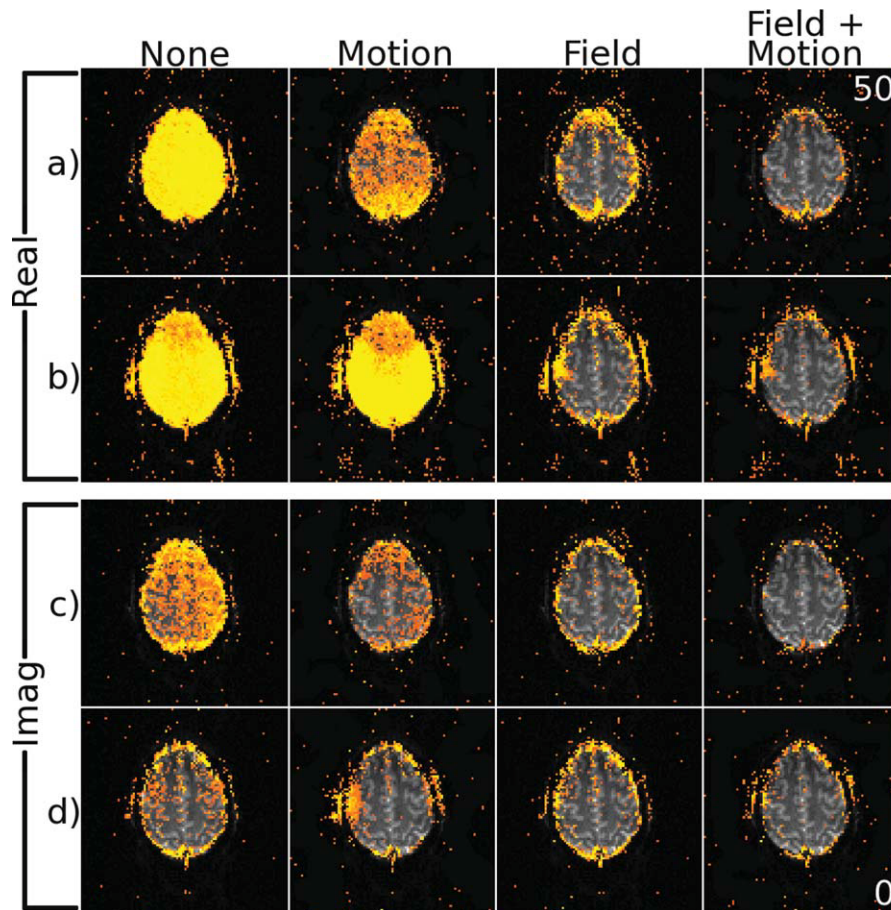


Figure 4.

Maps of the χ^2 statistics resulting from voxel-wise Breusch–Godfrey tests for autocorrelations in the real (a,b) and imaginary (c,d) residuals of complex-valued regression at a lag of 1 after different postprocessing steps. Significant voxels shown above a threshold of $P < 0.001$ (unadjusted). Results are shown for both EXPB (a,c) and EXPJ (b,d). [Color figure can be viewed in the online issue, which is available at wileyonlinelibrary.com.]

for removing the sample autocorrelation, while application of both consistently provides the minimum autocorrelation. It is worth noting that in the data from EXPJ remains significantly autocorrelated in part of the area above the jaw, even after full correction.

Voxel-wise analysis of the normality of the real and imaginary residuals from the complex-valued regression after the different postprocessing steps is displayed in Figure 5. Specifically shown are the results of an Anderson–Darling test [Anderson and Darling, 1952] in EXPB and EXPJ, which tests for deviations in the error from a normal distribution. In these images, voxels colored red represent those which reject the null hypothesis that the residuals belong to a normal distribution with probability $P < 0.01$. The Anderson–Darling test is used, because it has been shown to be one of the most powerful tests for deviations from normality [Stevens, 1974] and is on par with the Shapiro–Wilk test [Shapiro and Wilk, 1965], which is the test

employed by Luo and Nichols [2003]. Similar to the autocorrelations, it seems that application of both motion compensation and dynamic field correction provides the most desirable signal characteristics. However, in this case, either motion correction or field correction alone seem to provide nearly the same performance as the two combined, except in the case of the imaginary residuals from EXPJ. In that case, deviations from normality were the most severe, and the relative normality in the other cases may be the reason either correction alone performs as well as both together.

In EXPJ, there are a few areas that contain significantly autocorrelated and to a lesser extent non-normal residuals even after full correction. The greatest example of this can be seen in the real autocorrelations in Figure 4c. The failure to completely restore temporal independence and normality is likely twofold. First, the spatial variation in the field is very large in these areas and may not be

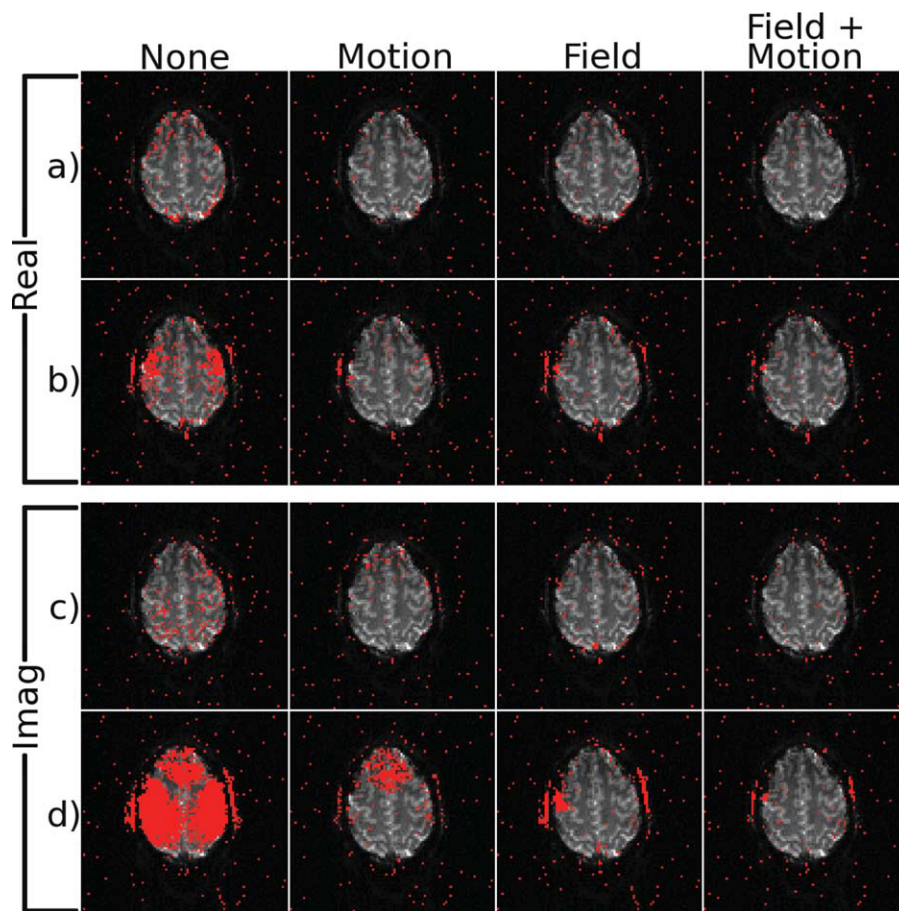


Figure 5.

Maps of the results from voxel-wise Anderson–Darling tests for deviations from normality in the distributions of the real (a,b) and imaginary (c,d) residuals of complex-valued regression after different postprocessing steps. Voxels that are colored red are those in

which the null hypothesis is rejected with probability $P < 0.01$ (unadjusted). Results are shown for both EXPB (a,c) and EXPJ (b,d). [Color figure can be viewed in the online issue, which is available at wileyonlinelibrary.com.]

fully captured by the model, thus leaving it partially uncorrected. Additionally, because of these large spatial variations, significant intravoxel effects are likely to be present, and this is not correctable with the TOAST method and is likely unrelated to bulk motion. It is interesting to note that the areas previously mentioned, which become active in EXPJ in the test of magnitude-and-or-phase after applying both corrections (Fig. 2f), coincide with locations where the autocorrelations and departures from normality are not fully removed. This combined with the relatively poor conditioning of the design matrix could explain why these areas become active in this case.

Simulation

Each of the 100 iterations of the simulated experiments SIMB and SIMJ were analyzed in exactly the same fashion

as the human experiments, EXPB and EXPJ. The SIMC iterations were only processed corresponding to the “none” case of the human experiments as no dynamic field offset nor motion was present. The results were analyzed by quantifying the detection power, which is defined as the number of iterations out of 100 in which a test statistic was significant at a specified threshold [Logan and Rowe, 2004; Logan et al., 2008]. For each set of tests, the threshold for each individual test matched that used in the human data analysis. Only voxels meeting this threshold in at least 5 of the 100 tests are shown in the images, masking away the others. This choice of thresholding was used to provide optimal comparability with the human results. Each of the images resulting from simulation represent voxels where the true mean of the distribution is shifted such that at least 5% of its area lies over the percentage corresponding to the specific single test threshold of the area under the null distribution curve. This way, the probability that an unmasked voxel would be significant

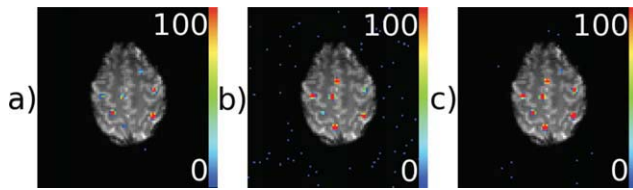


Figure 6.

Maps of the detection power for magnitude-only (a), phase only (b), and magnitude-and-or-phase (c) in the SIMC simulation. Voxels are shown when detection power is 5% or greater. Detection power is defined as the percentage of iterations a voxel tested significant at $P < 5 \times 10^{-4}$ (unadjusted). [Color figure can be viewed in the online issue, which is available at wileyonlinelibrary.com.]

in a single trial at its single trial threshold is the same regardless of that threshold.

The results of magnitude-only, phase-only, and magnitude-and-or-phase activation detection are shown in Figure 6 for the SIMC series and Figure 7 for SIMB and SIMJ. The results shown in Figure 7 present characteristics that appear to corroborate what was seen in the human data. First, magnitude-only activity (Fig. 7a,b) is not drastically different between various postprocessing steps, which is similar to the behavior of the experimental data, and it is arguable that the degree of variation in both simulated and acquired data is somewhat similar. Second, phase-only detection power in SIMB and SIMJ, shown in Figure 7c,d, is significantly reduced without dynamic field correction and reaches power levels near the control with the field correction applied. The relative effect of the motion compensation alone corresponds to some degree with the acquired data; in that, a small amount of power is recovered from the unprocessed case. It is of interest to note that the previously mentioned area, which becomes active outside of the motor cortex in EXPJ after applying both corrections, is not reproduced in SIMJ. This may be caused by the imperfect representation of the exact field changes or motion that occurred the lack of through plane field gradients in the simulation, or some other signal source present in the experimental data that was not included in the simulation. Finally, the magnitude-and-or-phase power in SIMB and SIMJ (Fig. 7e,f) show responses to postprocessing similar to those observed in experimental data in the majority of cases as well.

It should be noted that the detection power shown for SIMC is not expected to be achievable in either SIMB or SIMJ. The motion applied to both SIMB and SIMJ shifts the active locations around through time, and the motion compensation applied will not account for this. The correction for motion, which is applied, will simply remove variance in the signal that is correlated with the estimated motion. Achieving the smallest difference between the control and the test cases is still obviously the goal, however.

The temporal autocorrelations and distribution normality of the real and imaginary residuals following complex-valued regression after the different postprocessing steps in SIMB and SIMJ were investigated in the same manner as done for EXPB and EXPJ previously. The results of the voxel-wise Breusch–Godfrey test of temporal independence and the Anderson–Darling test of deviations from normality are shown in Figures 8 and 9, respectively. The same tests for SIMC resulted in no significance for either test beyond the expected type 1 errors and are not shown here.

The images in Figures 8 and 9 show that the simulated motion and magnetic field variations cause significant autocorrelation and deviations from normality as seen in experimental data. Additionally, the autocorrelations appear to be more problematic than non-normality in this case as well. The corrections also seem to have a similar impact in the simulated data as they do experimentally. In the autocorrelations, neither motion nor TOAST correction alone generally provide as good a result as the two together. The deviations from normality, when not very strong, appear to be corrected equally well by either motion or field correction alone, but across the board, the best results are achieved by applying both in tandem.

Beyond the similarities between simulated and experimental data in terms of how the corrections affect the temporal signal characteristics, there also seem to be similarities between the two with respect to the pattern of autocorrelation and non-normality. Connections between them can be seen in many cases, and this helps to support the validity of the simulation and the repeatability of the corrections.

DISCUSSION

The experimental and simulated data presented thus far have demonstrated the improvements that can be achieved with complex-valued fMRI analysis using TOAST and motion correction in situations containing known nuisance signals that are likely exaggerated compared to what will usually occur during a common fMRI experimental acquisition. Although this shows that this methodology can be beneficial in more extreme and difficult cases, it does not necessarily indicate the expected benefit in more common environments. As previously mentioned, a more typical fMRI acquisition was not included in the Results section above, so that the argument presented there relied on consistent, comparable data. Rather, a quick inspection of the complex-valued activation statistics after performing TOAST and motion correction in a fMRI time series acquired with more common parameters and without any nuisance task is presented here for the purposes of discussion.

Figure 10 shows the activations detected using the model for magnitude-only (Fig. 10a), phase-only (Fig. 10b), and magnitude-and-or-phase (Fig. 10c) in EXPC. The

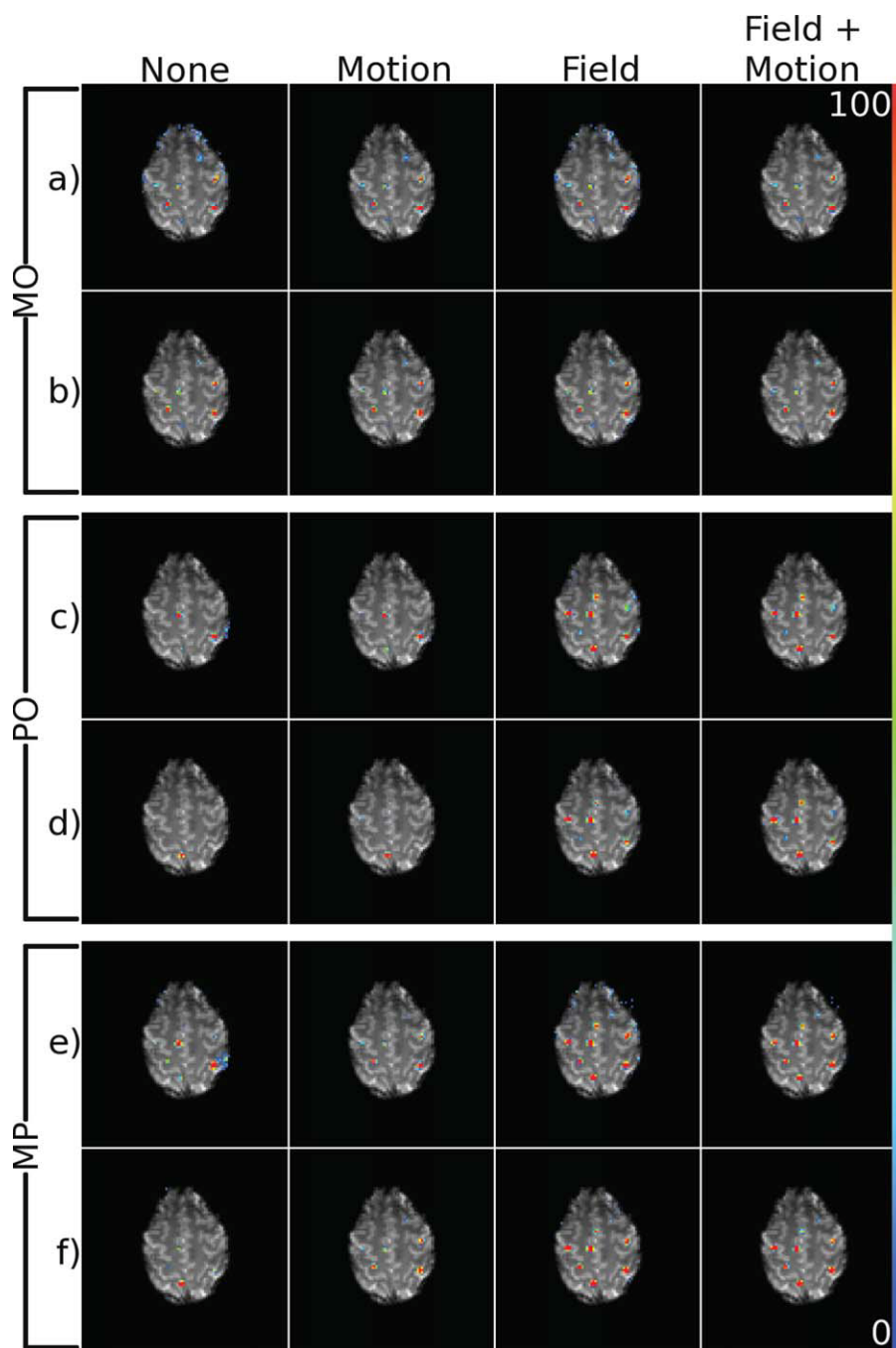


Figure 7.

Maps of the detection power for magnitude-only (a,b), phase-only (c,d), and magnitude-and-or-phase (e,f) activation. The results of SIMB (a,c,e) and SIMJ (b,d,f) are shown for each activation model. From left to right, columns show results after no postprocessing, motion compensation only, dynamic field correction only, and both motion and field correction. Voxels are

shown when detection power is 5% or greater. Detection power is defined as the percentage of iterations a voxel tested significant at $P < 5 \times 10^{-4}$ (unadjusted). [Color figure can be viewed in the online issue, which is available at wileyonlinelibrary.com.]

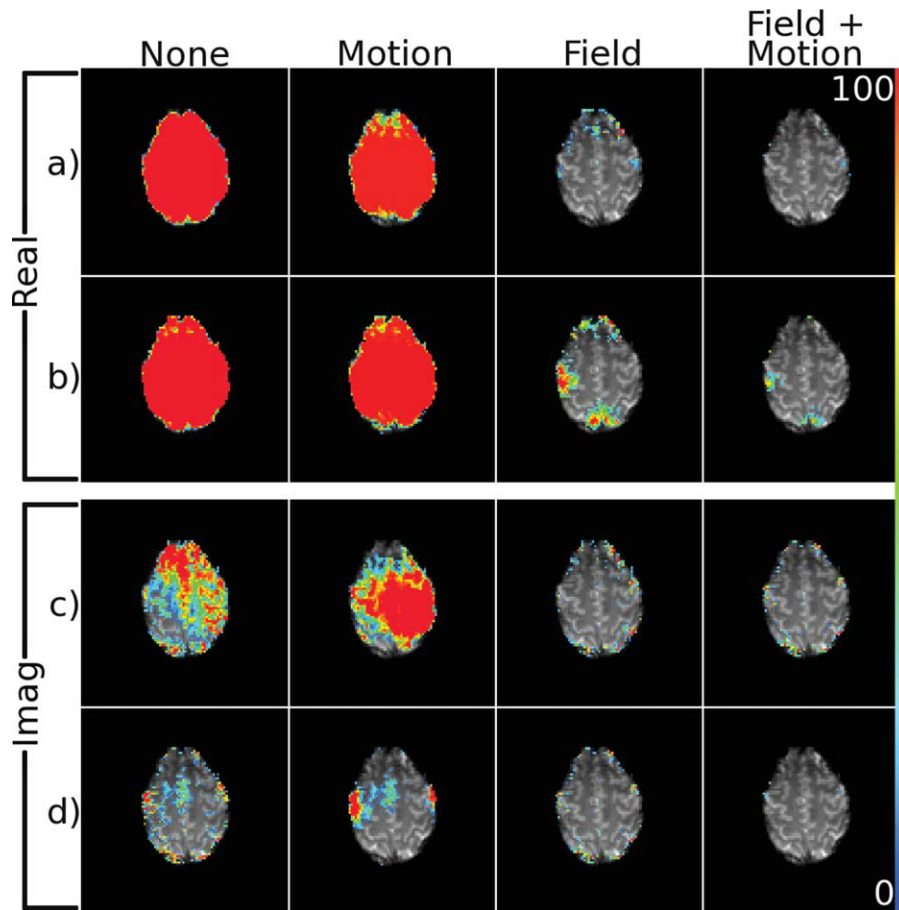


Figure 8.

Maps of the detection power for voxel-wise Breusch–Godfrey tests of autocorrelations in the real (a,b) and imaginary (c,d) residuals of complex-valued regression at a lag of 1 after different postprocessing steps. Voxels are shown when detection power is 5% or greater. Detection power is defined as the per-

centage of iterations a voxel tested significant at $P < 0.001$ (unadjusted). Results are shown for both SIMB (a,c) and SIMJ (b,d). [Color figure can be viewed in the online issue, which is available at wileyonlinelibrary.com.]

details of the acquisition of EXPC can be found in Table I and the Methods section above. The results of the magnitude-only statistics show behavior similar to what was observed in EXPB and EXPJ, that is, little difference between each case. Phase-only results are slightly more interesting. Around the motor cortex, the results are the same as those previous in that little to no activity is present without correction and applying TOAST and TOAST with motion correction yields activations in that area. However, without any correction, a large area of activity is detected in the anterior part of the brain that appears artifactual in nature. In this case, applying the corrections removes the significant activity in this area. Finally, the magnitude-and-or-phase activity is what is expected given the magnitude-only and phase-only data. Most importantly, the significance of activations in the expected areas, that is, motor cortex, is increased by the

corrections, while the activity in the anterior brain is reduced by them. In these final results, the activity in the motor cortex, although diminished, is present with no correction at all.

Two things can be said of these results. First, it appears that, some improvement, in terms of phase-only and complex-valued detection power, is possible using the two correction methods in this case. However, the degree of improvement, especially in the magnitude-and-or-phase activations, is diminished compared to that seen in EXPB and EXPJ, which is not unexpected. Second, the corrections seem to be beneficial with respect to removal of artifactual activity in this case, which was not necessarily the case in EXPB and EXPJ. It is hard to predict the occurrence of such artifacts, but it seems reasonable to think that these corrections could reduce their effects.

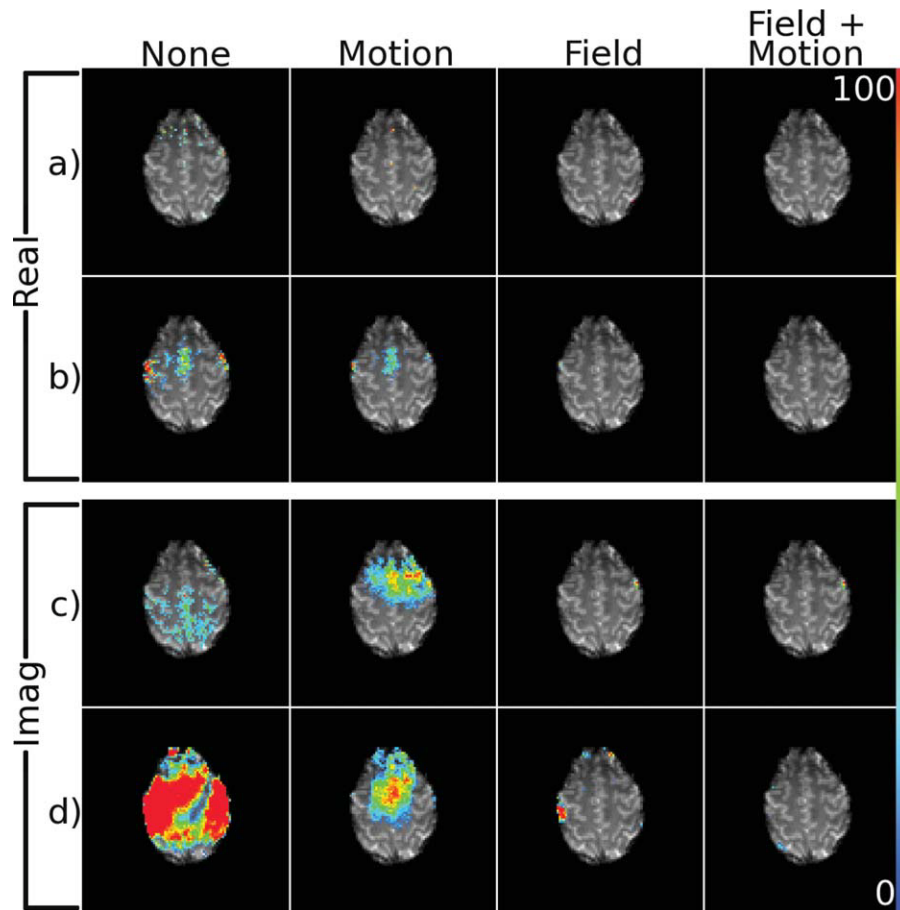


Figure 9.

Maps of the detection power for voxel-wise Anderson–Darling tests for deviations from normality in the distributions of the real (a,b) and imaginary (c,d) residuals of complex-valued regression after different postprocessing steps. Voxels are shown when detection power is 5% or greater. Detection power is

defined as the percentage of iterations a voxel tested significant at $P < 0.01$ (unadjusted). Results are shown for both SIMB (a,c) and SIMJ (b,d). [Color figure can be viewed in the online issue, which is available at wileyonlinelibrary.com.]

Rather than reduce artifacts, the use of both motion correction and field correction as opposed to simply field correction alone seemed to induce an artifact in EXPJ in the phase-only and magnitude-and-or-phase activations as previously mentioned, and it was suggested that ill-conditioning of the design matrix when including motion estimations as regressors may be a contributing factor. This potential ill-conditioning is a weakness associated with performing motion compensation in this way. Additionally, certain signal components may not arise due to motion, but motion regressors can, in certain situations, account for some of the signal, reducing the significance of the task reference regressor and thus the detection of true activation. It is possible that this problem may be eliminated through use of a motion correction scheme tailored for complex-valued fMRI data, and further work is necessary to determine whether this is feasible. However, the data seems to show in the other cases that even this

imperfect motion compensation seems to be beneficial in a general sense, and including it as a postprocessing correction still provides the best results. This certainly seems to be true with regard to residual temporal autocorrelations and non-normality.

The processing techniques used to enhance the complex-valued fMRI statistical analysis presented here represent only two of the potentially useful methods. The dynamic magnetic field correction appears to provide the foundation for the demonstrated improvements, and motion correction was included because of its common use in many fMRI experiments. Additionally, these two methods alone provide a significantly more optimal and robust time series, can be used without any special pulse sequence modifications or physiologic monitoring during experimentation, and thus may be applied to any EPI fMRI data set previously collected if the complex-valued images are available.

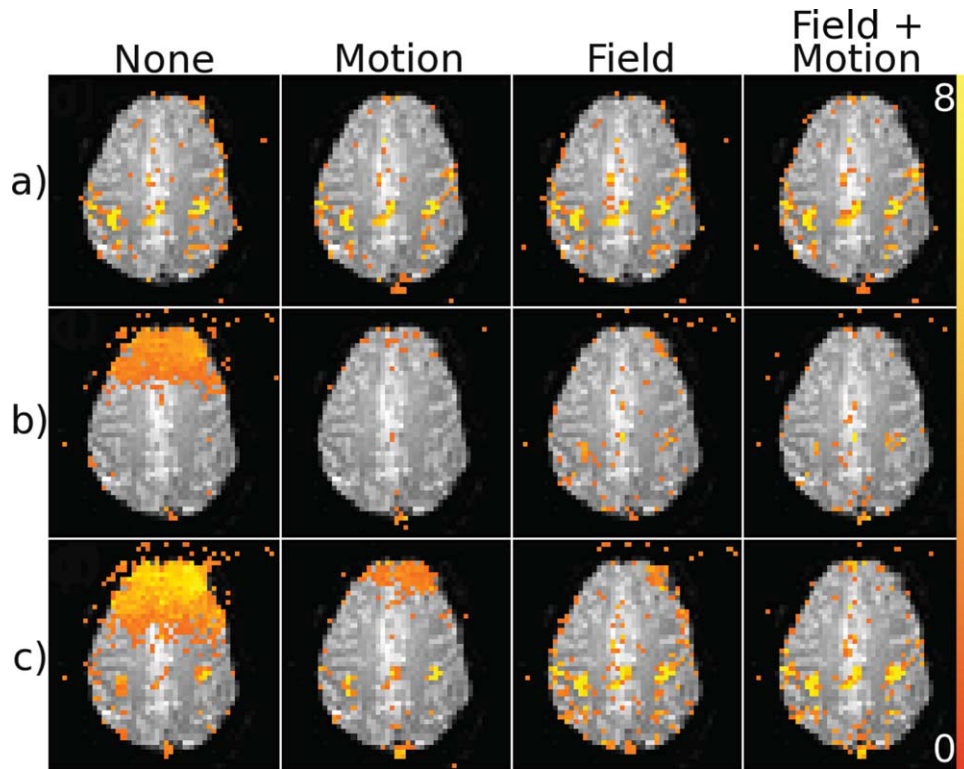


Figure 10.

Maps of $-\log_{10}P$, where P is the P -value associated with the χ^2 statistics for magnitude-only (a), phase-only (b), and magnitude-and-or-phase (c) activation in EXPC after different postprocessing corrections. Active voxels shown above a threshold of $P < 5 \times 10^{-4}$ (unadjusted). [Color figure can be viewed in the online issue, which is available at wileyonlinelibrary.com.]

Additional benefit may be realized by using time series representing unwanted signal components other than motion as nuisance regressors during statistical analysis. These may be based on respiration, heart rate, or any other physiologic process monitored during an experiment [Glover et al., 2000], or can be derived directly from the acquired data itself along with a short reference scan [Bianciardi et al., 2009; de Zwart et al., 2008]. Although the work of Glover et al. [2000], de Zwart et al. [2008], and Bianciardi et al. [2009] discuss application for magnitude-only data, extension to complex-valued data is possible in the same manner used for motion parameter regression in this work. This type of technique would likely complement the field correction well, providing the capability to compensate for detrimental signal, which is more spatially localized and often not associated with a bulk magnetization shift, such as cardiac-induced pulsatile blood flow or modulated blood oxygenation with respiration.

The complex-valued regression analysis used in this work is only applied in a very rudimentary and straightforward manner as a means of demonstrating the initial challenges facing the technique and its potential utility following the correction processes. Further work is necessary

to focus more on utilizing its flexibility to apply more appropriate complex-valued functional response models and investigate the complex-valued functional impulse response now that a foundation exists to consistently achieve a robust complex-valued time series.

CONCLUSION

The investigation of the practical utility of a complex-valued statistical model in fMRI data presented here is motivated by growing interest in both phase-only and magnitude and phase analysis. Results were presented from both human fMRI time series and simulated data demonstrating that phase-only and complex-valued regression analysis of raw fMRI time series is generally challenging and certainly suboptimal, due to large nuisance signal components in the phase. This does not imply that all complex-valued analysis of raw data is expected to be unreasonable or highly flawed, but that these issues exist and can potentially cause significant problems.

The results went on to demonstrate that applying dynamic magnetic field correction can significantly reduce

the effect of the unwanted signals, and motion correction can further improve the normality and temporal autocorrelation of the complex-valued time series. As a result, the complex-valued regression is much more powerful, and the simple tests and analysis provided in this work appear to indicate that valid and potentially valuable physiologic information is contained in the complex-valued fMRI signal.

REFERENCES

- Anderson TW, Darling DA (1952): Asymptotic theory of certain "goodness-of-fit" criteria based on stochastic processes. *Ann Math Stat* 23:193–212.
- Bandettini PA, Jesmanowicz A, Wong EC, Hyde JS (1993): Processing strategies for time-course data sets in functional MRI of the human brain. *Magn Reson Med* 30:161–173.
- Bandettini PA, Petridou N, Bodurka J (2005): Direct detection of neuronal activity with MRI: Fantasy, possibility, or reality? *Appl Magn Reson* 29:65–88.
- Belsley DA, Kuh E, Welsch RE (1980): *Regression Diagnostics: Identifying Influential Data and Sources of Collinearity*. New York: Wiley.
- Bianciardi M, van Gelderen P, Duyn JH, Fukunaga M, de Zwart JA (2009): Making the most of fMRI at 7 T by suppressing spontaneous signal fluctuations. *NeuroImage* 44:448–454.
- Birn RA, Bandettini PA, Cox RW, Jesmanowicz A, Shaker R (1998): Magnetic field changes in the human brain due to swallowing or speaking. *Magn Reson Med* 40:55–60.
- Bodurka J, Bandettini PA (2002): Toward direct mapping of neuronal activity: MRI detection of ultraweak, transient magnetic field changes. *Magn Reson Med* 47:1052–1058.
- Bodurka J, Jesmanowicz A, Hyde JS, Xu H, Estkowski L, Li S-J (1999): Current-induced magnetic resonance phase imaging. *J Magn Reson* 137:265–271.
- Breusch TS (1979): Testing for autocorrelation in dynamic linear models. *Aust Econom Pap* 17:334–355.
- Calhoun VD, Adali T, Pearlson GD, van Zijl PCM, Pekar JJ (2002): Independent component analysis of fMRI data in the complex domain. *Magn Reson Med* 48:180–192.
- Chow LS, Cook GG, Whitby E, Paley MNJ (2006): Investigation of mr signal modulation due to magnetic fields from neuronal currents in the adult human optic nerve and visual cortex. *Magn Reson Imaging* 24:681–691.
- Cleveland WS, Devlin SJ (1988): Locally-weighted regression: An approach to regression analysis by local fitting. *J Am Stat Assoc* 83:596–610.
- Cox RW (1996): Software for analysis and visualization of functional magnetic resonance neuroimages. *Comp Biomed Res* 29:162–173.
- de Zwart JA, van Gelderen P, Fukunaga M, Duyn JH (2008): Reducing correlated noise in fMRI data. *Magn Reson Med* 59:939–945.
- Durbin J, Watson GS (1971): Testing for serial correlation in least squares regression, Part 3. *Biometrika* 58:1–19.
- Feng Z, Caprihan A, Blagoev KB, Calhoun VD (2009): Biophysical modeling of phase changes in BOLD fMRI. *NeuroImage* 47:540–548.
- Glover GH, Li TQ, Ress D (2000): Image-based method for retrospective correction of physiological motion effects in fMRI: Retroicor. *Magn Reson Med* 44:162–167.
- Godfrey LG (1978): Testing against general autoregressive and moving average error models when the regressors include lagged dependent variables. *Econometrica* 46:1293–1302.
- Hagberg GE, Bianciardi M, Brainovich V, Cassarà AM, Maraviglia B (2008): The effect of physiological noise in phase functional magnetic resonance imaging: From blood oxygen level-dependent effects to direct detection of neuronal currents. *Magn Reson Imaging* 26:1026–1040.
- Hahn AD, Nencka AS, Rowe DB (2009): Improving robustness and reliability of phase-sensitive fMRI analysis using temporal off-resonance alignment of single-echo timeseries (TOAST). *NeuroImage* 44:742–752.
- Heller L, Barrowes B, George J (2007): Modeling direct effects of neural current on MRI. *Hum Brain Mapp* 30:1–12.
- Hernandez-Garcia L, Vazquez AL, Rowe DB (2009): Complex-valued analysis of arterial spin labeling based fMRI signals. *Magn Reson Med* 62:1597–1608.
- Hoogenraad FG, Reichenbach JR, Haacke EM, Lai S, Kuppusamy K, Sprenger M (1998): In vivo measurement of changes in venous blood-oxygenation with high resolution functional mri at 0.95 tesla by measuring changes in susceptibility and velocity. *Magn Reson Med* 39:97–107.
- Jesmanowicz A, Wong EC, Hyde JS (1993): Phase correction of EPI using internal reference lines. *Proc Soc Magn Reson Med* 12:1239.
- Johnstone T, Walsh KSO, Greischar LL, Alexander AL, Fox AS, Davidson RJ, Oakes TR (2006): Motion correction and the use of motion covariates in multiple-subject fMRI analysis. *Hum Brain Mapp* 27:779–88.
- Kadah YM, Hu X (1997): Simulated phase evolution rewinding (sphere): A technique for reducing b0 inhomogeneity effects in mr images. *Magn Reson Med* 38:615–627.
- Konn D, Leach S, Gowland P, Bowtell R (2004): Initial attempts at directly detecting alpha wave activity in the brain using MRI. *Magn Reson Imaging* 22:1413–1427.
- Lai S, Glover G (1997): Detection of BOLD fMRI signals using complex data. *Proc Int Soc Magn Reson Med* 5:1671.
- Lee J, Shahram M, Schwartzman A, Pauly JM (2007): Complex data analysis in high-resolution SSFP fMRI. *Magn Reson Med* 57:905–917.
- Logan BR, Rowe DB (2004): An evaluation of thresholding techniques in fMRI analysis. *NeuroImage* 22:95–108.
- Logan BR, Geliakova MP, Rowe DB (2008): An evaluation of spatial thresholding techniques in fMRI analysis. *Hum Brain Mapp* 29:1379–1389.
- Luo W, Nichols TE (2003): Diagnosis and exploration of massively univariate neuroimaging models. *NeuroImage* 19:1014–1032.
- Menon RS (2002): Postacquisition suppression of large-vessel bold signals in high-resolution fMRI. *Magn Reson Med* 47:1–9.
- Nan FY, Nowak RD (1999): Generalized likelihood ratio detection for fmri using complex data. *IEEE Trans Med Imaging* 18:320–329.
- Nencka AS, Rowe DB (2007): Reducing the unwanted draining vein bold contribution in fMRI with statistical post-processing methods. *NeuroImage* 37:177–188.
- Ogawa S, Lee TM, Kay AR, Tank DW (1990): Brain magnetic resonance imaging with contrast dependent on blood oxygenation. *Proc Natl Acad Sci USA* 87:9868–9872.
- Petridou N, Plenz D, Silva AC, Loew M, Bodurka J, Bandettini PA (2006): Direct magnetic resonance detection of neuronal electrical activity. *Proc Natl Acad Sci USA* 103: 16015–16020.
- Rowe DB (2005a) Parameter estimation in the magnitude-only and complex-valued fMRI data models. *NeuroImage* 25:1124–1132.

- Rowe DB (2005b) Modeling both the magnitude and phase of complex-valued fMRI data. *NeuroImage* 25:1310–1324.
- Rowe DB (2009): Magnitude and Phase Signal Detection in Complex-valued fMRI Data. *Magn Reson Med* 62:1356–1357.
- Rowe DB, Logan BR (2004): A complex way to compute fMRI activation. *NeuroImage* 23:1078–1092.
- Rowe DB, Logan BR (2005): Complex fMRI analysis with unrestricted phase is equivalent to a magnitude-only model. *NeuroImage* 24:603–606.
- Rowe DB, Nencka AS (2006): Complex activation suppresses venous BOLD in GE-EPI fMRI data. *Proc Soc Magn Reson Med* 14:2834.
- Rowe DB, Meller CP, Hoffmann RG (2007): Characterizing phase-only fMRI data with an angular regression model. *J Neurosci Methods* 161:331–341.
- Shapiro SS, Wilk MB (1965): An analysis of variance test for normality (complete samples). *Biometrika* 62:591–611.
- Soltysik DA, Hyde JS (2006): Strategies for block-design fMRI experiments during task-related motion of structures of the oral cavity. *NeuroImage* 29:1260–1271.
- Stevens MA (1974): EDF statistics for goodness of fit and some comparisons. *J Am Stat Assoc* 69:730–737.
- Sundaram P, Wells WM, Mulkern RV, Bubrick EJ, Bromfield EB, Munch M, Orbach EB (2010): Magnetic resonance imaging of cerebral electromagnetic activity in epilepsy. *Proc Int Soc Magn Reson Med* 18:441.
- Zhao F, Jin T, Wang P, Hu X, Kim S-G (2007): Sources of phase changes in bold and cbv-weighted fMRI. *Magn Reson Med* 57:520–527.
- Zhu H, Li Y, Ibrahim JG, Shi X, An H, Chen Y, Gao W, Lin W, Rowe DB, Peterson BS (2009): Regression models for identifying noise sources in magnetic resonance images. *J Am Stat Assoc* 104:623–637.